AGU100 ADVANCING EARTH AND SPACE SCIENCE

Geophysical Research Letters

RESEARCH LETTER
10.1029/2018GL077891

Key Points:
- Virga precipitation occurrence percentage is quantified by three spaceborne radars
- The virga precipitation occurrence percentage is over 30% (50%) by both PR and DPR (CPR) over arid regions
- The virga precipitation accounts for ~50% (30%) of false precipitation detection by TMI (GMI) over arid regions

Correspondence to:
Y. You,
yyou@umd.edu

Citation:
Wang Y., You, Y., & Kulie, M. (2018). Global virga precipitation distribution derived from three spaceborne radars and its contribution to the false radiometer precipitation detection. *Geophysical Research Letters*, *45*, 4446–4455. https://doi.org/10.1029/2018GL077891

Received 14 MAR 2018
Accepted 15 APR 2018
Accepted article online 1 MAY 2018
Published online 9 MAY 2018

Global Virga Precipitation Distribution Derived From Three Spaceborne Radars and Its Contribution to the False Radiometer Precipitation Detection

Yu Wang[1], **Yalei You**[2], **and Mark Kulie**[3]

[1]School of Earth and Space Sciences, University of Science and Technology of China, Hefei, China, [2]Earth System Science Interdisciplinary Center/Cooperative Institute for Climate and Satellites, University of Maryland, College Park, MD, USA, [3]Department of Geological and Mining Engineering and Sciences, Michigan Technological University, Houghton, MI, USA

Abstract This study first quantifies the virga precipitation occurrence percentage using three spaceborne radar observations, including Tropical Rainfall Measuring Mission Precipitation Radar (PR), Global Precipitation Measurement dual-frequency PR (Ku-band PR/Ka-band PR [KuPR/KaPR]), and CloudSat Cloud Profiling Radar (CPR). PR and KuPR/KaPR show that virga occurrence percentage is over 30% in arid regions (e.g., Sahara desert and deserts of Australia). CPR reveals similar virga geospatial distribution. However, the virga percentage based on CPR is about twice as large as that based on PR and KuPR/KaPR due to better detection sensitivity. Results also show that the majority of the virga clouds are altostratus and cirrus. Second, we investigate the virga precipitation contribution to the passive microwave radiometer false precipitation detection. Virga precipitation accounts for as much as 50% (30%) of Tropical Rainfall Measuring Mission Microwave Imager (Global Precipitation Measurement Microwave Imager) false detection results in arid regions. The underlying reason is because precipitation detection over land primarily relies on the ice scattering signature, while virga and light precipitation (e.g., 1 mm/hr) have similar amounts of ice water path in arid regions.

Plain Language Summary Virga precipitation is defined as the "wisps or streaks of water or ice particles falling out of a cloud but vaporizing before reaching the earth's surface as precipitation." We show the global virga precipitation occurrence percentage using three spaceborne radar observations. Virga precipitation occurrence percentage is over 30% in arid regions (e.g., Sahara desert, Arabian Peninsula, and deserts of Australia), with the largest values over the Sahara desert. In addition, the virga precipitation is often misidentified as the precipitation on the ground by passive microwave radiometer, which is a key instrument to map the global precipitation. We show that virga precipitation accounts for as much as 50% of the false precipitation detection results in the arid regions.

1. Introduction

Virga precipitation is defined as the *wisps or streaks of water or ice particles falling out of a cloud but vaporizing before reaching the earth's surface as precipitation*, according to American Meteorological Society, Glossary of Meteorology (Glickman, 2000). Several previous works investigated this phenomenon using ground radar observations. For example, Rosenfeld and Mintz (1988) showed that all liquid water hydrometeors evaporate by 1.6 km below the cloud base with the rain rate at the cloud base being 1 mm/hr, based on the observations from one station during one summer season in South Africa. They also found that for moderate and very heavy rain intensities at the cloud base, the hydrometeors also respectively evaporate by 50% and 25% by 1.6 km below the cloud base. By using ground radar observations from three locations, Evans et al. (2011) showed that virga precipitation widely existed during the 1998–2004 drought period over the Canadian Prairies. Previous studies also investigated the regional virga precipitation characteristics using the Precipitation Radar (PR) on board the Tropical Rainfall Measuring Mission (TRMM) satellite (Kummerow et al., 1998), which was launched in late 1997 with the coverage from 36°S to 36°N. Geerts and Dejene (2005) concluded that about 28% of the radar profiles are virga precipitation over the Sahara desert region, compared with about 10% virga profiles over the Amazon region. Saikranthi et al. (2014) pointed out that virga precipitation occurs more frequently over the Indian subcontinent than over its adjoining oceans. The Cloud Profiling Radar (CPR)

on board the CloudSat satellite, launched in April 2006 with coverage from 82°S to 82°N, has also been used to study virga precipitation. For example, Hudak et al. (2008) showed that virga precipitation profiles contribute to about one fourth (27 out of 107) of the overall misidentified precipitation profiles by using CPR and one Canadian C band ground radar observations. In addition, the Dual-frequency Precipitation Radar (DPR) (Ku-band PR and Ka-band PR [KuPR/KaPR]) on board the Global Precipitation Measurement (GPM) satellite, launched in March 2014 with the coverage from 65°S to 65°N, provides new opportunities to investigate virga precipitation features.

The first objective of this study is to quantify the virga precipitation occurrence percentage using three spaceborne radars, including the TRMM PR, GPM DPR (KuPR and KaPR), and CloudSat CPR. Second, we quantify the contribution of virga precipitation to passive microwave radiometer false precipitation detection. Precipitation estimation from passive microwave radiometers serves as the key input to the widely used gridded hourly (half-hourly) global precipitation map, for example, Integrated Multi-Satellite Retrievals (Huffman et al., 2015), National Oceanic and Atmospheric Administration Climate Prediction Center Morphing technique (Xie et al., 2017), and Global Satellite Mapping of Precipitation (Kubota et al., 2007). To obtain an accurate precipitation estimate from passive microwave radiometers, it is essential to correctly detect precipitation. It has long been recognized that certain surfaces over land—such as snow cover and desert—may have a similar scattering signature as precipitation. There are extensive studies in the literature to screen out these land surfaces to avoid possible false precipitation detection (Ferraro & Marks, 1995; Grody, 1991; Seto et al., 2005; Turk et al., 2014; You, Wang, et al., 2017). On the other hand, the brightness temperature (TB) observed by the radiometer is directly proportional to the water path (the integrated hydrometeors in the air), not to the surface precipitation rate (e.g., You & Liu, 2012). In other words, virga precipitation, for which the hydrometeors do not reach the ground, is possibly misidentified as surface precipitation. Therefore, the second objective of this study is to quantify how often virga precipitation causes false precipitation detection in passive microwave radiometer retrievals.

2. Data

This study uses three types of data sets, including radar observations, passive microwave radiometer-estimated surface precipitation rates, and radiometer-observed TBs. The radar data are from TRMM PR, GPM KuPR and KaPR, and CloudSat CPR. We use the full record of PR observations from December 1997 to April 2015 and KuPR/KaPR observations from March 2014 to December 2017. Since CloudSat experienced a battery anomaly in April 2011 and is in day-only operation mode since November 2011, we only use CPR observations from April 2006 to April 2011. Table 1 provides some basic characteristics of these three radars.

For all three spaceborne radars, we use the radar reflectivity profile, near-surface reflectivity and retrieved near-surface precipitation rate. The near surface is defined as the surface closest to the ground without ground clutter. Specifically, CloudSat defines the near-surface bin height as the sixth (fifth) range gate above land (ocean) surfaces or about 1.44 (1.2) km above ground (sea) level. Both PR and DPR are scanning radars. The near-surface bin can range from ~1 km (nadir and near-nadir scans) to ~2.5 km (furthest off-nadir scans) above ground/sea level. Due to the larger bin height value at the off-nadir scans and also the possible mismatch between off-nadir radar observations and radiometer observations, this study only uses PR and DPR nadir observations.

Because spaceborne radar precipitation rates use the near-surface bin as a proxy for surface precipitation, this study probably underestimates virga events due to the near-surface blind zone, whereby evaporation/sublimation can occur between the near-surface bin height and the surface. Alternatively, the instantaneous satellite observation only provides a snapshot picture, while the hydrometers may fall to ground after the observation. This study may overestimate virga events under such circumstances. High spatial and temporal ground-based radar observations can mitigate these issues. However, ground radar observations are limited in the regional scale.

We also use the ice water path (IWP), contained in the PR 2A25 and KuPR 2ADPR products, to explain why virga precipitation may cause false radiometer precipitation detection over land. We choose to show IWP since the land precipitation detection primarily depends on the ice scattering signal (Ferraro et al., 1998; You et al., 2011, You, Peters-Lidard, et al., 2017)

Table 1
Characteristics of TRMM PR, GPM DPR (KuPR/KaPR), and CloudSat CPR

Instrument	TRMM PR	GPM KuPR/KaPR	CloudSat CPR
Frequency (GHz)	13.8	13.6/35.55	94.05
Minimum detection (dBZ)	17	12/12	−30
Horizontal resolution (nadir, km)	4.3[a]	5.2/5.2	1.4 × 1.8
Vertical resolution (m)	250	125/250	500
Spatial coverage	36°S–36°N	65°S–65°N	82°S–82°N
Temporal coverage	12/1997–4/2015	3/2014–	4/2006–4/2011[b]

Note. TRMM = Tropical Rainfall Measuring Mission; PR = Precipitation Radar; GPM = Global Precipitation Measurement; CPR = Cloud Profiling Radar; DPR = dual-frequency PR; KuPR = Ku-band PR; KaPR = Ka-band PR.
[a]Nadir resolution increased to 5 km with the satellite altitude increase in August 2001. [b]CloudSat experienced a battery anomaly in April 2011 and is in day-only operation mode since November 2011.

The surface precipitation detection results from the TRMM Microwave Imager (TMI) and GPM Microwave Imager (GMI) are used to show virga precipitations contribution to the false radiometer (TMI and GMI) precipitation detection. To further understand why virga precipitation could result in the false precipitation detection, the vertically polarized TB at 85.5 GHz (hereafter V85) from TMI and vertically polarized TB at 166 GHz (hereafter V166) from GMI are used in this study. The pixel resolution for V85 and V166 is approximately 5 × 7 km. We choose these two channels since they are the most sensitive channels to ice particle scattering from TMI and GMI, respectively. The 183.3-GHz channels from GMI are also very sensitive to the ice particle scattering. However, the water vapor effect reduces their scattering signature (Bennartz & Bauer, 2003; You, Wang, et al., 2017). We also analyze other widely used scattering signature indicators, for example, the scattering index (Grody, 1991) and the polarization-corrected temperature (Spencer et al., 1989). The results are very similar to those based on V85 and V166.

To collocate PR and V85 observations, we simply find the closest V85 pixel to match each PR nadir observation, due to the similar footprint size between PR and V85. Using the same method, the TMI precipitation detection result is collocated with PR observations. Similarly, we find the closest V166 pixels and GMI precipitation detection result to match each KuPR nadir observation.

It is worth mentioning that the TRMM satellite altitude increase from 350 to 402.5 km in August 2001 has very little influence for rainfall detection and intensity estimation (Shimizu et al., 2009). In our analysis and computations, we verified that there is no difference by using both the TRMM preboost and postboost data periods.

All variables used in this study are from TRMM, GPM, and CloudSat latest version products. Specifically, for PR, we use the 2A25 data set (version 7), which includes radar reflectivity profiles, near-surface reflectivity, near-surface precipitation rate, and IWP. For TMI, we use 1B11 (version 7) and 2A12 (version 7), which include 85-GHz TB and surface precipitation detection results, respectively. For GMI, we use 1BGMI (version 5) and 2AGPROF (version 5), which include 166-GHz TB and surface precipitation detection results, respectively. For DPR, we use 2ADPR 1B11 (version 5), which includes radar reflectivity profile, near-surface reflectivity, near-surface precipitation rate, and IWP. For CPR, we use 2B-GEOPROF (version 5), which includes radar reflectivity profiles and near-surface reflectivity. We also use 2C-SNOW-PROFILE (version 4) to obtain the near-surface snowfall rate. To analyze the virga cloud type, we use the 2B-CLDCLASS (version 4) product.

3. Virga Precipitation Definition

The three radars used in this study have different minimum detection threshold values (Table 1). For PR, KuPR, and KaPR, we define virga precipitation as the surface reflectivity is less than the minimum detection threshold value, while there is at least one layer in the air with a reflectivity value larger than or equal to the minimum detection threshold. For example, the virga precipitation based on the PR is that the surface reflectivity is less than 17 dBZ, while there is at least one reflectivity value in the atmospheric column is larger than or equal to 17 dBZ.

For CPR, previous work showed that CPR observations with near-surface reflectivity greater than −15 dBZ indicates the existence of the precipitating clouds (e.g., Haynes et al., 2009; Kawamoto & Suzuki, 2013;

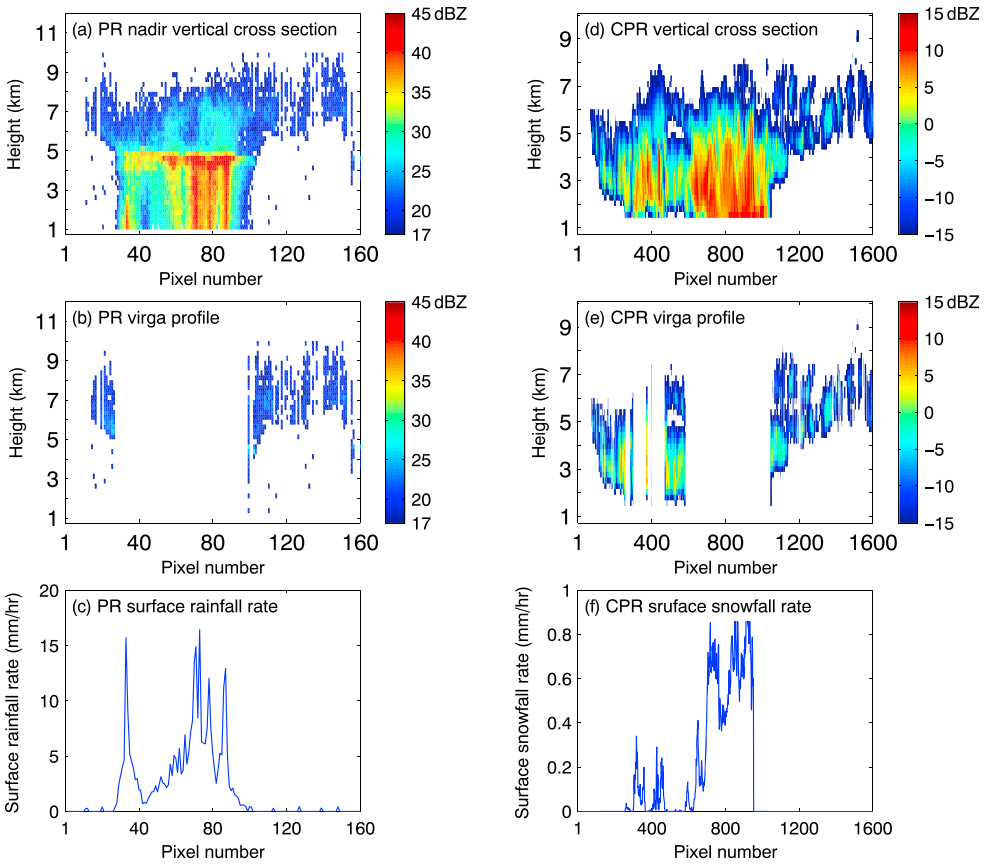

Figure 1. (a) Tropical Rainfall Measuring Mission PR nadir vertical cross section on 12 October 2002, over North Pacific (latitude: 31.5°N–33.5°N, longitude: 145°E–153°E). (b) Virga profiles in (a). (c) Surface rain rate corresponding to (a). (d) CPR vertical cross section on 20 September 2006, over Alaska and adjacent ocean (latitude: 68°N–78°N, longitude: 100°W–160°W). (e) Virga profiles in (d). (f) Surface snowfall rate corresponding to (c). PR = Precipitation Radar; CPR = Cloud Profiling Radar.

Leon et al., 2008; Stephens & Haynes, 2007). On the other hand, it is known that heavy precipitation can significantly attenuate CPR signal. In other words, a CPR profile with near-surface reflectivity less than −15 dBZ could also be a precipitating profile due to the strong attenuation from heavy rainfall. Therefore, we define the virga precipitation from CPR as the surface reflectivity is less than −15 dBZ, while there is at least one layer in the air with a reflectivity value greater than or equal to −15 dBZ but less than 10 dBZ. We choose 10 dBZ as the threshold value by using 3-year collocated data between PR and CPR from 2008 to 2010. When CPR near-surface reflectivity is less than −15 dBZ and PR detects near-surface rainfall (possible strong attenuation), a large majority (73.32%) of the maximum reflectivity in a CPR profile is larger than 10 dBZ. These profile types are considered as precipitating profiles, although the near-surface reflectivity is less than −15 dBZ.

In the following section, we compute the virga percentage by comparing with precipitating profiles. Therefore, it is necessary to clearly define precipitating profiles. For PR and DPR, the precipitating profile is defined as follows: The surface reflectivity is greater than or equal to the minimum detection threshold value (see Table 1). For CPR, a profile is judged as the precipitating profile when (a) the surface reflectivity is greater than or equal to −15 dBZ or (b) there is at least one layer in the air with the reflectivity greater than or equal to 10 dBZ, even if the near-surface reflectivity is less than −15 dBZ. The surface reflectivity below −15 dBZ in the latter scenario is judged due to strong attenuation caused by heavy precipitation in the air.

Figure 1a shows the nadir PR vertical cross section of a virga case on 12 October 2002 over the North Pacific Ocean (latitude: 31.5°N–33.5°N, longitude: 145°E–153°E). Elevated hydrometeors exist in the atmosphere from profile 10 to 28 and from 100 to 160 (Figure 1b). However, the surface rain rate in Figure 1c is 0, indicating that these hydrometeors do not reach the ground. Figure 1d shows the CPR vertical cross section of a virga case on 20 September 2006 over Alaska and the adjacent ocean (latitude: 68°N–78°N, longitude:

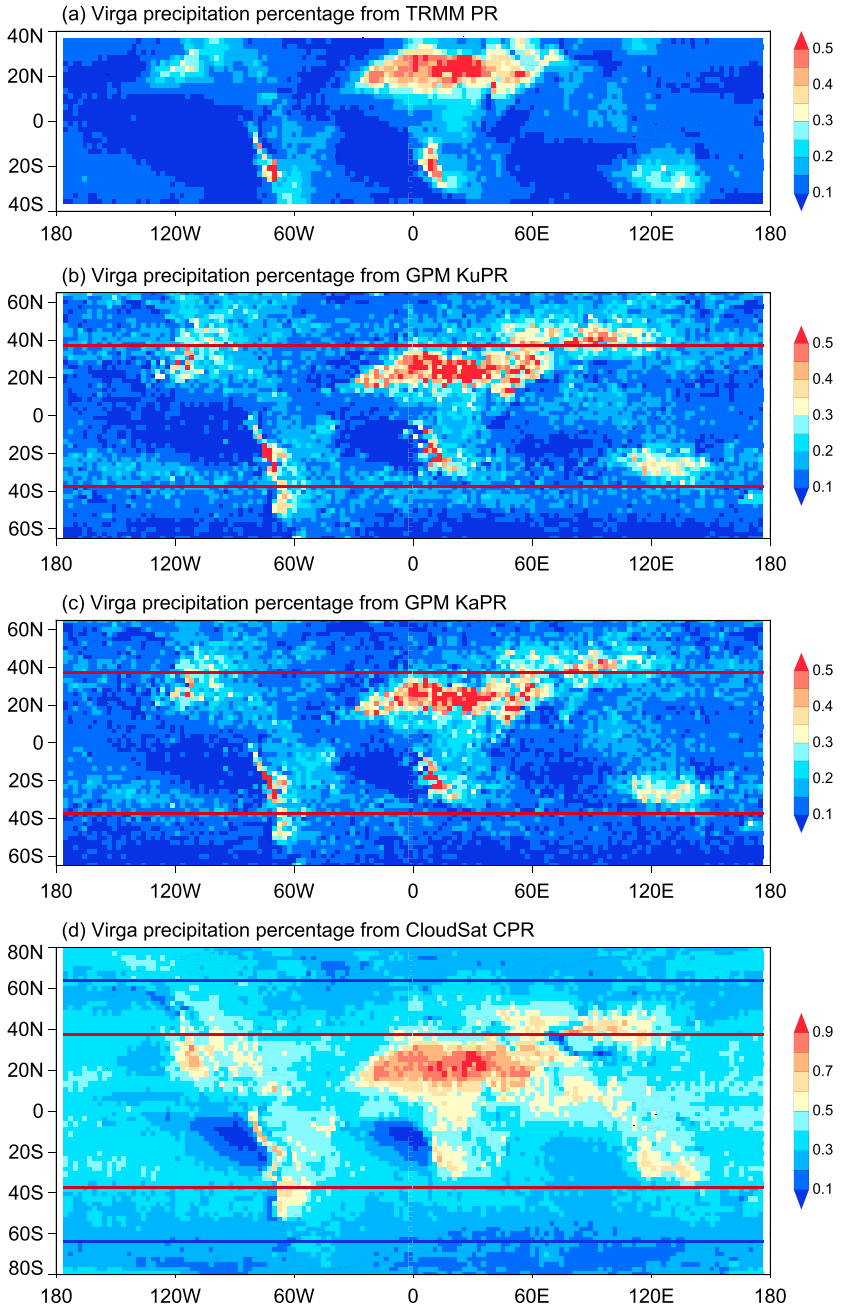

Figure 2. From top to bottom: virga occurrence percentage derived from PR, KuPR, KaPR, and CloudSat PR. The virga occurrence percentage is defined as the number of the virga precipitation events in each 2.5° grid box divided by the sum of combined virga precipitation and surface precipitation observations. The red solid lines from (b) to (d) correspond to 36°S and 36°N, respectively (TRMM PR-covered region). The blue solid lines in (d) correspond to the 65°S and 65°N, respectively (KuPR/KaPR-covered region). PR = Precipitation Radar; GPM = Global Precipitation Measurement; KuPR = Ku-band PR; KaPR = Ka-band PR; TRMM = Tropical Rainfall Measuring Mission.

100°W–160°W). The virga identification is shown in Figure 1e. It is clear that these virga profile in Figure 1e does not produce surface snowfall rate, by comparing Figures 1e and 1f.

It is cautioned that PR cannot observe any hydrometeor with reflectivity less than 17 dBZ, due to its sensitivity limitation. We show later that the virga precipitation occurrence percentage depends on the minimum detection threshold value, but the geospatial distribution of the virga precipitation is consistent from all radars.

4. Virga Precipitation Occurrence Percentage

The virga precipitation occurrence percentage is defined as the number of the virga precipitation events in each 2.5° grid box divided by the sum of combined virga precipitation and surface precipitation observations. We show the occurrence percentage, instead of the absolute number of the virga occurrence, because these three satellites (TRMM, GPM, and CloudSat) have more samples in the higher latitudes due to orbital characteristics. Figure 2a shows the virga percentage derived from PR. It is clear that the largest virga occurrence percentage is located over the Sahara desert regions, with the percentage larger than 50%. Other arid regions, including the deserts of Australia, Arabian Peninsula, Iran, and western United States also have virga percentages greater than 30%. The virga percentage is less than 20% over the vast majority of the ocean. There are several areas over ocean, adjacent to arid land areas, with a virga percentage of about 30% (e.g., the ocean regions west of California and the Sahara desert). Several previous studies reported that radar reflectivity profiles over land decrease strongly at lower altitudes largely due to stronger evaporation (Hirose & Nakamura, 2004; Liu & Fu, 2001; Liu & Zipser, 2013; You & Liu, 2012). This effect contributes to the more frequent virga occurrence over land. Additionally, the updraft over land is much stronger than over ocean (e.g., Williams & Stanfill, 2002), which contributes to much more frequent virga occurrences over land.

Both KuPR and KaPR show very similar virga percentage geospatial pattern in the TRMM-covered region (38°S–38°N; two red lines in Figures 2b and 2c). However, the virga percentage from KuPR and KaPR in the TRMM-covered region is slightly larger than that from PR, which is particularly evident over Australia. The improved detection KuPR/KaPR sensitivity leads to the slightly larger virga occurrence percentage. Beyond the TRMM-covered region, the large virga occurrence percentage over the dry areas is also evident in Figures 2b and 2c, for example, the Gobi desert in Northwest China and Patagonia in the southern portion of South America.

Although the geospatial distribution is largely similar, the virga occurrence percentage derived from the CPR (Figure 2d) is almost twice as large as that from the PR, KuPR, and KaPR due to the much smaller minimum detection threshold value (Table 1). According to the CloudSat cloud type data set (2B-CLDCLASS), virga clouds can be grouped into following eight categories with the percentage shown in the parentheses: altostratus (48.01%), cirrus (20.06%), altocumulus (10.94%), nimbostratus (9.13%), stratocumulus (8.68%), cumulus (1.63%), deep convection (1.55%), and stratus (0.002%). Surprisingly, virga clouds could also be deep convection and nimbostratus, which are possible surface precipitating cloud categories according to 2B-CLDCLASS. Case studies show that a CPR profile may be classified as nimbostratus or deep convection clouds by the 2B-CLDCLASS algorithm, even though there is no surface precipitation associated with that profile. This situation can arise since the 2B-CLDCLASS product independently assesses surface precipitation potential from other CloudSat products like 2C-RAIN-PROFILE or 2C-SNOW-PROFILE. For example, a virga profile may be classified as a deep convective cloud when this profile is embedded within a larger contiguous convective system. Further analysis shows that a large majority of virga is less than 1,000 km away from dense, towering vertical cloud, which are often considered as anvil clouds, similar to the cloud shape in Figures 1a and 1d.

In summary, the virga precipitation occurrence percentage is over 30% in arid regions based on PR, KuPR, and KaPR observations, with the largest virga occurrence percentage over the Sahara desert region. The CPR virga percentage is almost doubled due to much better detection sensitivity.

5. Virga Precipitation's Contribution to the False Radiometer Precipitation Detection

This section uses the collocated radiometer observations between TMI and PR, and between GMI and KuPR to investigate the virga precipitation's contribution to the overall TMI and GMI false precipitation detection results. The KaPR results are almost identical to that from KuPR; therefore, only the KuPR results are shown. Additionally, CloudSat CPR and Advanced Microwave Scanning Radiometer for Earth Observing System onboard the Aqua satellite have observations less than 120 s apart. However, we do not use Advanced Microwave Scanning Radiometer for Earth Observing System observations because the rainfall detection algorithm screens out a large portion of the arid regions over land, where virga precipitation occurs most frequently.

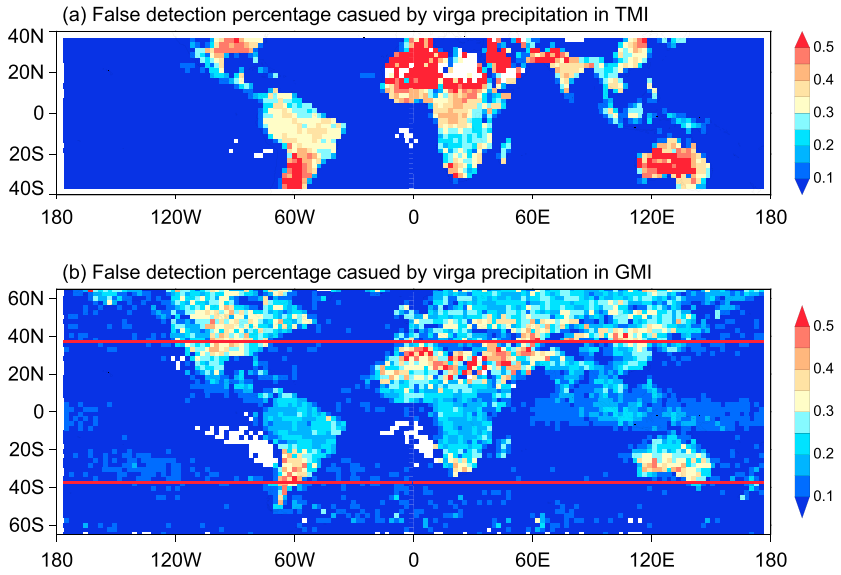

Figure 3. (a) The percentage of the false precipitation detection in the TMI detection result, caused by the virga precipitation. (b) Same as (a) except in the GMI detection result. The red solid lines in (b) corresponds to 36°S and 36°N, respectively (Tropical Rainfall Measuring Mission Precipitation Radar–covered region). TMI = Tropical Rainfall Measuring Mission Microwave Imager; GMI = Global Precipitation Measurement Microwave Imager.

Figure 3 shows the TMI false detection percentage caused by virga precipitation (Figure 3a) and GMI (Figure 3b) precipitation detection results (Figure 3b) in each 2.5° grid box, where PR and KuPR are taken as the reference, respectively. The false detection is defined as when a pixel is judged as a nonprecipitating pixel by PR (KuPR), while it is judged as a precipitating pixel by TMI (GMI; Kummerow et al., 2011; Seto et al., 2005; Wang et al., 2009). In each 2.5° grid box, we first count how many pixels are false detection pixels (N1). Second, we count how many pixels out of these false detection pixels are associated with virga precipitation (N2). The false detection percentage caused by virga precipitation is calculated as N2/N1.

It is known that both N1 and N2 may change, according to different referenced instruments (Berg et al., 2002; Kummerow et al., 2011). For example, a precipitating pixel judged by GMI may be considered as a false detection if KuPR is used as the reference instrument. On the other hand, this may be a correct detection by GMI

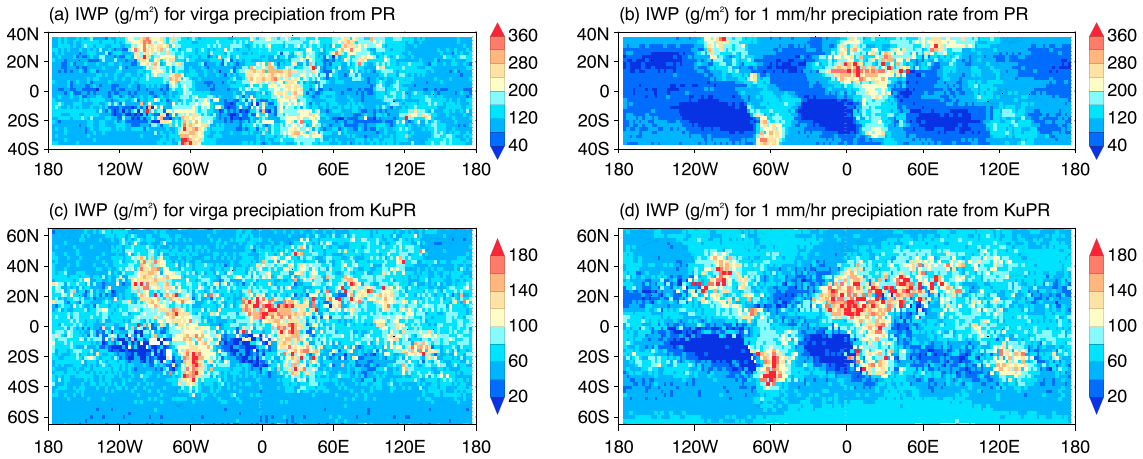

Figure 4. (a) Mean ice water path (IWP) corresponding to the virga precipitation in each 2.5° grid box, derived from PR. (b) Mean IWP corresponding to 1-mm/hr surface precipitation rate in each 2.5° grid box, derived from PR. (c) Mean IWP corresponding to the virga precipitation in each 2.5° grid box, derived from KuPR. (d) Mean IWP corresponding to 1-mm/hr surface precipitation rate in each 2.5° grid box, derived from KuPR. PR = Precipitation Radar; KuPR = Ku-band PR.

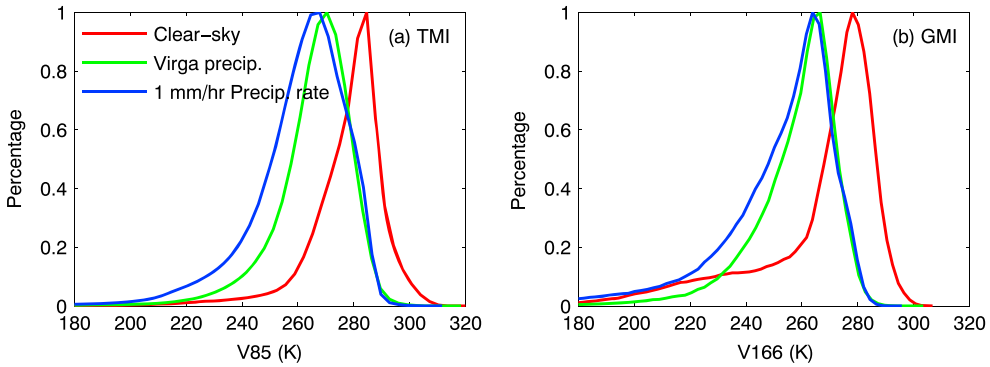

Figure 5. (a) Histogram of V85 from TMI corresponding to clear sky (red curve), the virga precipitation (green curve), and 1-mm/hr surface precipitation rate (blue curve). (b) Histogram of V166 from GMI corresponding to clear sky (red curve), the virga precipitation (green curve), and 1-mm/hr surface precipitation rate (blue curve). GMI = Global Precipitation Measurement Microwave Imager; TMI = Tropical Rainfall Measuring Mission Microwave Imager.

if CPR is taken as the reference. However, this study computes the percentage value (N2/N1), instead of the absolute values of N1 and N2, which remains roughly the same regardless of the reference instruments.

Figure 3a shows that virga precipitation systematically causes false precipitation detections in the TMI precipitation results. Virga accounts for over 30% of the overall false detections in the vast majority of the land regions. Particularly, over half of the false detection is caused by the virga precipitation over arid regions (e.g., Sahara desert, Arabian Peninsula, and deserts of Australia). Figure 3b shows the virga precipitation's contribution to the false precipitation detection in the GMI precipitation results. Over the arid regions, the false detection caused by virga is still large at ~30%.

To explain why the virga precipitation may be falsely identified as surface precipitation, we compare IWP from virga precipitation events with IWP from 1-mm/hr surface precipitation events based on PR and KuPR. We choose 1-mm/hr surface precipitation rate to represent the precipitation. Selecting another value (e.g., 0.5 mm/hr) does not change the conclusions. Figures 4a and 4b show the IWP, corresponding respectively to virga precipitation and 1-mm/hr surface precipitation rate from the PR. It is immediately clear that the IWP amount from virga can be larger than that from 1-mm/hr rainfall in some regions (e.g., central Africa). Therefore, the virga precipitation could result in larger TB depressions, which makes it almost impossible to distinguish them using microwave radiometer TBs.

To further illustrate this point, we further show the TMI V85 TB histogram in Figure 5a. The green curve from the virga precipitation and the blue curve from 1-mm/hr surface precipitation rate largely overlap each other, indicating that TB cannot reliably separate these two situations. As a reference, Figures 5a and 5b also show the histogram of TB under clear sky (red curve).

Similar to the TMI result, the KuPR IWP amount for virga precipitation can be larger than that from 1-mm/hr rainfall in some regions (e.g., central Africa, Amazon region, and Southeast Asia; cf. Figures 4c and 4d), making it difficult to separate the virga precipitation from the light precipitation (e.g., 1 mm/hr). Similarly, Figure 5b shows that V166 TB once again overlaps the virga precipitation (green curve in Figure 5b) and 1-mm/hr surface precipitation rate (blue curve in Figure 5b).

In summary, we show that the virga precipitation accounts for about 50% (30%) of false precipitation detection over arid regions in the TMI (GMI) precipitation detection results. The reason for these large false detections caused by virga is that both virga and light precipitation have very similar IWP values, which TB directly measures.

6. Conclusions and Discussions

This study first uses TRMM PR, GPM KuPR and KaPR, and CloudSat CPR observations to quantify virga precipitation occurrence percentage. Results show that virga precipitation occurrence percentage is over 30% in arid regions when PR, KuPR, and KaPR are analyzed. The largest virga occurrence percentage is located in the Sahara desert region, with percentages consistently larger than 50%. CPR observations show that the virga

precipitation occurrence percentage is about twice as large as that from PR, KuPR, and KaPR data sets, due to the much better CPR detection capability. In addition, results from this study also show that there is a much larger virga occurrence percentage over land than over ocean.

Second, we show that the virga precipitation accounts for about 50% (30%) of overall false precipitation events in the TMI (GMI) precipitation detection results in arid regions. The primary signature for precipitation detection over land is the TB depression caused by columnar ice scattering, but virga and light precipitation are shown to have very similar IWP values. Therefore, it is almost impossible to distinguish the virga precipitation from the light precipitation by only using the TBs.

Acknowledgments
TRMM and GPM data were downloaded from NASA PPS at https://storm.pps.eosdis.nasa.gov/storm/. CloudSat data were download from CloudSat data processing center at http://www.cloudsat.cira.colostate.edu/data-products/. This work is supported by the Ministry of Science and Technology of China (grant 2017YFC1501402) and the National Natural Science Foundation of China (grant 41375030). We thank the constructive and valuable comments from two anonymous reviewers. We also thank Zhien Wang at University of Wyoming for helpful information of ClouSat 2B-CLDCLASS product.

References

Bennartz, R., & Bauer, P. (2003). Sensitivity of microwave radiances at 85–183 GHz to precipitating ice particles. *Radio Science*, *38*(4), 8075.

Berg, W., Kummerow, C., & Morales, C. (2002). Differences between east and west Pacific rainfall systems. *Journal of Climate*, *15*(24), 3659–3672.

Evans, E., Stewart, R., Henson, W., & Saunders, K. (2011). On precipitation and virga over three locations during the 1999–2004 Canadian Prairie drought. *Atmosphere-Ocean*, *49*(4), 366–379.

Ferraro, R. R., & Marks, G. F. (1995). The development of SSM/I rain-rate retrieval algorithms using ground-based radar measurements. *Journal of Atmospheric and Oceanic Technology*, *12*(4), 755–770.

Ferraro, R. R., Smith, E. A., Berg, W., & Huffman, G. J. (1998). A screening methodology for passive microwave precipitation retrieval algorithms. *Journal of the Atmospheric Sciences*, *55*(9), 1583–1600.

Geerts, B., & Dejene, T. (2005). Regional and diurnal variability of the vertical structure of precipitation systems in Africa based on spaceborne radar data. *Journal of Climate*, *18*(7), 893–916.

Glickman, T. (2000). *Glossary of meteorology*. MA, USA: American Meteorological Society.

Grody, N. C. (1991). Classification of snow cover and precipitation using the special sensor microwave imager. *Journal of Geophysical Research*, *96*(D4), 7423–7435.

Haynes, J. M., L'Ecuyer, T. S., Stephens, G. L., Miller, S. D., Mitrescu, C., Wood, N. B., & Tanelli, S. (2009). Rainfall retrieval over the ocean with spaceborne W-band radar. *Journal of Geophysical Research*, *114*, D00A22. https://doi.org/10.1029/2008JD009973

Hirose, M., & Nakamura, K. (2004). Spatiotemporal variation of the vertical gradient of rainfall rate observed by the TRMM precipitation radar. *Journal of Climate*, *17*, 3378–3397.

Hudak, D., Rodriguez, P., & Donaldson, N. (2008). Validation of the CloudSat precipitation occurrence algorithm using the Canadian C band radar network. *Journal of Geophysical Research*, *113*, D00A07. https://doi.org/10.1029/2008JD009992

Huffman, G. J., Bolvin, D. T., Braithwaite, D., Hsu, K., Joyce, R., Xie, P., & Yoo, S.-H. (2015). NASA Global Precipitation Measurement (GPM) Integrated multi-satellitE Retrievals for GPM (IMERG). *Algorithm theoretical basis document, version*, *4*, 1–30.

Kawamoto, K., & Suzuki, K. (2013). Comparison of water cloud microphysics over mid-latitude land and ocean using CloudSat and MODIS observations. *Journal of Quantitative Spectroscopy and Radiative Transfer*, *122*, 13–24.

Kubota, T., Shige, S., Hashizume, H., Aonashi, K., Takahashi, N., Seto, S., et al. (2007). Global precipitation map using satellite-borne microwave radiometers by the GSMaP project: Production and validation. *IEEE Transactions on Geoscience and Remote Sensing*, *45*(7), 2259–2275.

Kummerow, C., Barnes, W., Kozu, T., Shiue, J., & Simpson, J. (1998). The Tropical Rainfall Measuring Mission (TRMM) sensor package. *Journal of Atmospheric and Oceanic Technology*, *15*(3), 809–817.

Kummerow, C. D., Ringerud, S., Crook, J., Randel, D., & Berg, W. (2011). An observationally generated a priori database for microwave rainfall retrievals. *Journal of Atmospheric and Oceanic Technology*, *28*(2), 113–130.

Leon, D. C., Wang, Z., & Liu, D. (2008). Climatology of drizzle in marine boundary layer clouds based on 1 year of data from CloudSat and Cloud-Aerosol Lidar and Infrared Pathfinder Satellite Observations (CALIPSO). *Journal of Geophysical Research*, *113*, D00A14. https://doi.org/10.1029/2008JD009835

Liu, G., & Fu, Y. (2001). The characteristics of tropical precipitation profiles as inferred from satellite radar measurements. *Journal of the Meteorological Society of Japan*, *79*(1), 131–143.

Liu, C., & Zipser, E. J. (2013). Why does radar reflectivity tend to increase downward toward the ocean surface, but decrease downward toward the land surface? *Journal of Geophysical Research: Atmospheres*, *118*(1), 135–148. https://doi.org/10.1029/2012JD018134

Rosenfeld, D., & Mintz, Y. (1988). Evaporation of rain falling from convective clouds as derived from radar measurements. *Journal of Applied Meteorology*, *27*(3), 209–215.

Saikranthi, K., Narayana Rao, T., Radhakrishna, B., & Rao, S. (2014). Morphology of the vertical structure of precipitation over India and adjoining oceans based on long-term measurements of TRMM PR. *Journal of Geophysical Research: Atmospheres*, *119*, 8433–8449. https://doi.org/10.1002/2014JD021774

Seto, S., Takahashi, N., & Iguchi, T. (2005). Rain/no-rain classification methods for microwave radiometer observations over land using statistical information for brightness temperatures under no-rain conditions. *Journal of Applied Meteorology*, *44*(8), 1243–1259.

Shimizu, S., Tagawa, T., Iguchi, T., & Hirose, M. (2009). Evaluation of the effects of the orbit boost of the TRMM satellite on PR rain estimates. *Journal of the Meteorological Society of Japan*, *87*, 83–92.

Spencer, R. W., Goodman, H. M., & Hood, R. E. (1989). Precipitation retrieval over land and ocean with the SSM/I: Identification and characteristics of the scattering signal. *Journal of Atmospheric and Oceanic Technology*, *6*(2), 254–273.

Stephens, G. L., & Haynes, J. M. (2007). Near global observations of the warm rain coalescence process. *Geophysical Research Letters*, *34*, L20805. https://doi.org/10.1029/2007GL030259

Turk, F. J., Haddad, Z. S., & You, Y. (2014). Principal components of multifrequency microwave land surface emissivities. Part I: Estimation under clear and precipitating conditions. *Journal of Hydrometeorology*, *15*(1), 3–19.

Wang, N.-Y., Liu, C., Ferraro, R., Wolff, D., Zipser, E., & Kummerow, C. (2009). TRMM 2A12 land precipitation product-status and future plans. *Journal of the Meteorological Society of Japan*, *87*(0), 237–253.

Williams, E., & Stanfill, S. (2002). The physical origin of the land–ocean contrast in lightning activity. *Comptes Rendus Physique*, *3*(10), 1277–1292.

Xie, P., Joyce, R., Wu, S., Yoo, S.-H., Yarosh, Y., Sun, F., & Lin, R. (2017). Reprocessed, bias-corrected CMORPH global high-resolution precipitation estimates from 1998. *Journal of Hydrometeorology*, *18*(6), 1617–1641.

You, Y., & Liu, G. (2012). The relationship between surface rainrate and water paths and its implications to satellite rainrate retrieval. *Journal of Geophysical Research*, *117*, D13207. https://doi.org/10.1029/2012JD017662

You, Y., Liu, G., Wang, Y., & Cao, J. (2011). On the sensitivity of Tropical Rainfall Measuring Mission (TRMM) microwave imager channels to overland rainfall. *Journal of Geophysical Research*, *116*, D12203. https://doi.org/10.1029/2010JD015345

You, Y., Peters-Lidard, C., Turk, J., Ringerud, S., & Yang, S. (2017). Improving overland precipitation retrieval with brightness temperature temporal variation. *Journal of Hydrometeorology*, *18*(9), 2355–2383.

You, Y., Wang, N.-Y., Ferraro, R., & Rudlosky S. (2017). Quantifying the snowfall detection performance of the GPM microwave imager channels over land. *Journal of Hydrometeorology*, *18*(3), 729–751.